RSC Advances

PAPER

View Article Online
View Journal | View Issue

Cite this: *RSC Adv.*, 2026, **16**, 8695

Tetrad or triad? insights from a versatile Fe(II) structural and functional model of the 3-histidine 1-carboxylate tetrad in C–C bond cleaving dioxygenase enzymes

Adam Fadul,[a] Thomas Cundari,[b] Jeffery Bertke[c] and Santiago A. Toledo*[a]

Received 16th December 2025
Accepted 4th February 2026

DOI: 10.1039/d5ra09716a

rsc.li/rsc-advances

A new N_3O coordinate ferrous complex modeling the 3-histidine-1-carboxylate tetrad – a dioxygenase active site – was synthesized and crystallographically characterized, ([Fe(II)(*N*-(ethyl-*N*′Me2)(Py)(2-*t*-ButPhOH))(OTf)]), **1**. Complex **1** displays versatile C–C bond cleavage activity towards 2-hydroxyacetophenone, 3-hydroxyflavone, and 3,3-dihydroxypentan-2,4-dione in the presence of O_2. This reactivity was studied through UV-vis and NMR spectroscopy alongside DFT calculations. The latter suggests that **1** forms an Fe(III)O_2 adduct during the oxidation of 2-hydroxyacetophenone. Additionally, **1** displays direct activation of O_2 in the absence of substrate, allowing it to access reactivity akin to more traditional N_2O enzymatic coordination motifs. This versatility points to the need to reconsider mechanisms in N_3O coordinate enzymatic systems and biomimetic models thereof. Moreover, this research makes the case that carefully designed N_3O complexes merit further investigation as functional mimics of the canonical non-heme iron dioxygenase enzyme coordination environment.

Introduction

Dioxygenase enzymes are a broad class of proteins facilitating the incorporation of dioxygen into organic substrates.[1] These enzymes perform a wide range of chemical transformations across all living organisms, fulfilling essential functions including metabolism, hormone synthesis, and xenobiotic degradation.[2–5] With few exceptions, dioxygenase enzymes leverage the properties of transition metal cofactors to enable this exquisite chemistry. Transition metals such as cobalt, manganese, nickel, and copper are all known cofactors in dioxygenase enzymes; however, iron is the most common, particularly among mammalian enzymes.[6,7] Iron-containing dioxygenase enzymes are further classified into three categories: heme, Rieske, and mononuclear iron dioxygenase enzymes.[8,9] The work discussed herein is principally focused on the latter category.

Mononuclear iron dioxygenase enzymes contain an iron cofactor coordinated to endogenous protein-based ligands. These ligands are most typically histidine residues ligating the metal through imidazole N donors, and/or glutamate/aspartate residues ligating the metal through their side chain carboxylate moieties.[10] These protein-based ligands give rise to characteristic coordination environments, supporting the ability of the metal cofactor to enable dioxygenase chemistry.[11] The most common of these coordination motifs is a so-called 2-His-1-carboxylate facial triad coordinated to a ferrous iron center.[12] To date, over one hundred enzymes have been identified containing the 2-His-1-carboxylate structural motif, constituting an enzymatic superfamily first coined by Hegg and Que.[11,12] The 2-His-1-carboxylate superfamily of enzymes was defined in large part due to the highly conserved nature of the N_2O coordination motif in enzymes facilitating the direct activation of dioxygen. Enzymes such as the extradiol catechol dioxygenase family exhibit evidence for catalytically active Fe(II) superoxide radical species formed from the direct activation of O_2, promoted by bidentate binding of catechol substrate. The catalytically active species then facilitates aromatic C–C bond cleavage in the substrate.[13,14] Other enzymes, such as the family of aromatic amino acid hydroxylases (subgroup of intermolecular dioxygenase enzymes), are understood to form catalytically active Fe(IV)-oxo species wherein the direct activation of O_2 is promoted by a change in coordination mode of the endogenous glutamate residue from monodentate to bidentate. The catalytically active species then facilitates the hydroxylation of aromatic amino acid rings.[15,16] Enzyme families such as these served to underscore the flexibility of the 2-His-1-carboxylate facial triad in that they can stabilize a variety of low and high-valent oxidizing species derived from the activation of O_2 by the iron center.

---

[a] Department of Chemistry, American University, 4400 Massachusetts Ave NW, Washington, DC, 20016, USA. E-mail: stoledo@american.edu

[b] Department of Chemistry, University of North Texas, 1155 Union Cir, Denton, Texas 76203, USA

[c] Department of Chemistry, Georgetown University, 3700 O St NW, Washington, DC, 20057, USA

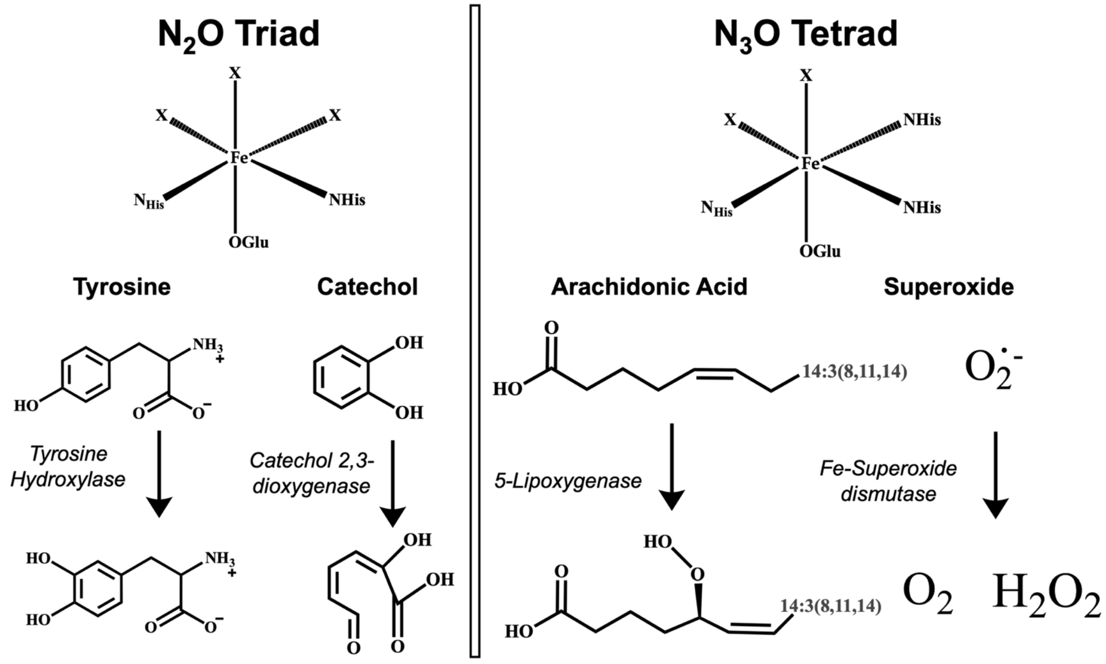

Fig. 1 Generic coordination of the 2-His-1-carboxylate triad (left) and 3-His-1-carboxylate tetrad (right) with relevant enzymes and substrates.

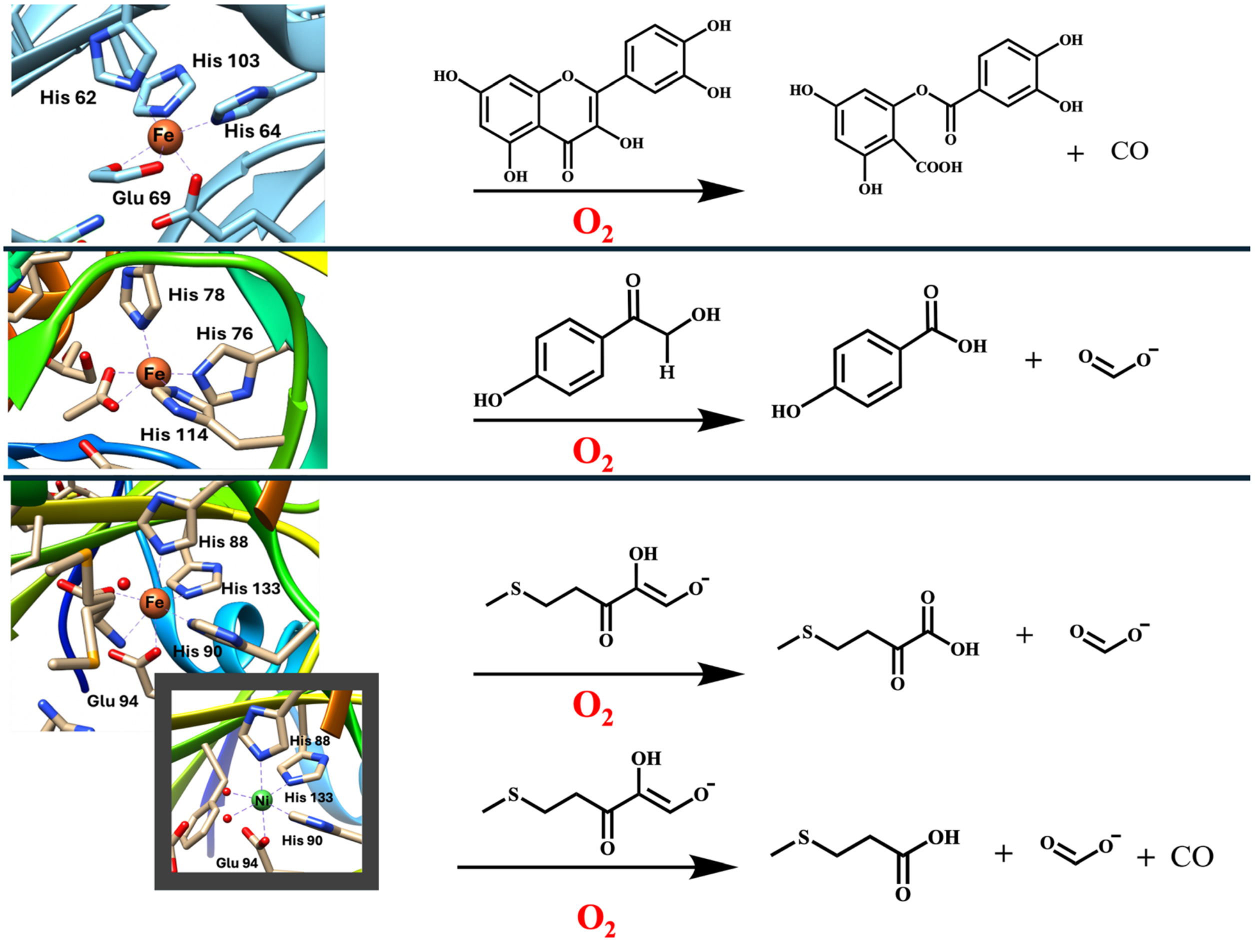

Fig. 2 Active sites (top to bottom) of iron containing QDO (PDB ID: 2H0V), DAD (PDB ID: 5BPX), Fe-ARD (PDB ID: 4QGN) and Ni-ARD (PDB ID: 5I8S) alongside their corresponding substrates and dioxygenation reaction products.

At the time the 2-His-1-carboxylate motif (N_2O) was defined in literature, enzymatic systems with more encumbered coordination motifs such as the 3-His-1-carboxylate tetrad (N_3O) (Fig. 1-right), were thought to lack the capacity for direct activation of dioxygen.[11] Enzymes such as the N_3O coordinate soybean lipoxygenase or iron-containing superoxide dismutase supported this notion in that neither enzyme exhibits the capacity for direct dioxygen activation.[17–20] Since the entrance of the 2-His-1-carboxylate facial triad into the canonical understanding of dioxygenase enzyme chemistry, additional enzymes containing a 3-His-1-carboxylate tetrad motif, such as acireductone dioxygenase (ARD) and quercetin dioxygenase (QDO), have been discovered with their mechanistic peculiarities garnering considerable attention in the literature.[21–25] ARD facilitates the penultimate step of the methionine salvage pathway, catalyzing the oxygen-mediated cleavage of the C1–C2 bond of the substrate 1,2-dihydroxo-3-keto-5-(thiomethyl)pent-1-ene (acireductone), yielding 2-keto-4-(thiomethyl) butyrate (KMBT) and formate. This reactivity is observed in iron-bound Fe-ARD in what is termed an "on pathway" reaction (Fig. 2-third scheme).[26,27] Interestingly, Ni, Mn, and Co-ARD isoforms of the very same enzyme are understood to facilitate an alternative "off pathway" reaction through both C1–C2 and C2–C3 bond cleavage in acireductone substrate, yielding 3-(methylthio) propionate (MTP), formate, and carbon monoxide (Fig. 2- third scheme).[27] QDO facilitates polyphenol degradation, catalyzing oxygen-mediated C2–C3 and C3–C4 bond cleavage in the substrate 3,3′,4′,5,7-pentahydroxyflavone (quercetin), yielding 2-protocatechuoyl phloroglucinol carboxylic acid (2PCPGCA) and carbon monoxide (Fig. 2-first scheme).[28–30] Like ARD, QDO exhibits notable metal promiscuity with QDO readily binding an array of transition metals.[31] However, unlike ARD, the various metal isoforms of QDO are understood to catalyze the same pattern of C–C bond cleavage.[32] The mechanisms of dioxygen activation in ARD and QDO are at present subjects of intense debate, with multiple possible mechanistic pathways having been presented in the literature, including direct activation of dioxygen by the metal cofactor.[6,32–35] Enzymatic studies have suggested a non-redox active role for the metal center in Ni-ARD, while computational and experimental evidence point to a possible redox active role for the metal center in Fe-ARD.[35–37] Evidence for the redox nature of the metal center in Co and Mn-ARD isoforms is at present mixed. In the case of QDO, computational work has suggested a non-redox active role for all QDO metal centers, while biomimetic studies have suggested possible redox active roles in Fe and Co-QDO.[32,33,38] In addition to ARD and QDO, the enzyme 2,4′-dihydroxyacetophenone dioxygenase (DAD) (Fig. 2-second scheme) has also garnered attention in literature for its role in oxygen-mediated cleavage of the aliphatic C1–C2 bond in the substrate 2,4′-dihydroxyacetophenone, albeit in an N_3 rather than N_3O coordinate system.[39,40] The enzymes ARD, QDO, and DAD are also related by the presence of an α-hydroxy ketone moiety in their respective substrates.

In this work, we introduce a versatile Fe(II)N_3O coordinate complex capable of biomimetic, dioxygen-mediated C–C bond cleavage in substrate analogs for the enzymes ARD, QDO, and DAD. This complex is also capable of direct O_2 activation. The breadth of reactivity observed in the Fe(II)N_3O complex exemplifies the flexibility of an atypical N_3O coordination motif and lays the foundation for future mechanistic studies of its reactivity that may elucidate alternative mechanisms and plausible reactivities for atypically coordinated enzymatic systems.

Experimental

Materials and methods

The preparation and manipulation of air-sensitive compounds were performed using standard Schlenk techniques and glove boxes under an N_2 atmosphere. Reagents and solvents were purchased from commercial suppliers of the highest available purity and used without further purification unless otherwise noted. Solvents were purchased ultra-dried and further dried using 4 Å molecular sieves (butanone and methanol). For acetonitrile, dichloroethane, and diethyl ether, the solvents were purified *via* a drying column on a PPTechnologies solvent purification system. Deuterated solvents were degassed *via* freeze–pump–thaw cycles. ^{1}H-NMR spectra were recorded on a Bruker Avance Core 400 MHz spectrometer at room temperature and referenced to a residual deuterated solvent. Quantitative ^{1}H-NMR was done by the addition of a known quantity of 1,3,5-trimethoxybenzene as an internal standard. The Evan's method was conducted following previously reported literature procedures.[41] UV-Visible spectra were recorded in a 1 cm cuvette on an Agilent Cary 60 spectrometer. Low-temperature UV-visible studies were collected using a Unisoku Cryostat USP-203-B: with a liquid Nitrogen reservoir and Temperature Controller. Cyclic voltammograms were recorded anaerobically using a Pine Research WaveNow Wireless potentiostat in a tetrabutylammonium hexafluorophosphate solution in acetonitrile (0.1 M) using a 2.0 mm glassy carbon working electrode, an Ag^+/$AgNO_3$ reference electrode, and a platinum auxiliary electrode. The detection of carbon monoxide was performed using literature procedures using the $AgNO_3$ method for the detection of low concentrations of carbon monoxide.[42] Elemental analyses were performed by Galbraith Atlantic Microlabs, Norcross, GA. ESI-MS experiments were conducted in partnership with the University of Maryland-College Park Mass-Spectrometry facility using a Bruker Maxis-II Q-TOF mass spectrometer. The samples were dissolved in acetonitrile prior to analysis. Synthetic procedures and characterization details are presented in the SI. The ligand *N*,*N*-(2-pyridil)(2-hydroxy-3-tbutylphenol)-*N*′-dimethylethane ((*N*-(ethyl-*N*′Me_2)-(Py)-(2-*t*-ButPhOH))-L1) was synthesized and purified as previously reported.[43]

Computational techniques

Density functional theory simulations employed the Gaussian 16 software package. The B3LYP functional and 6-31+G(d) basis sets were used for geometry optimizations and to confirm that the stationary points had the appropriate number of imaginary frequencies. For more accurate energetics, single-point calculations were performed at all stationary points at the B3LPY + GD3BJ/6-311++G(d,p)/SMD-acetonitrile level of theory.

Enthalpic and entropic corrections to electronic energies were derived from the unscaled B3LYP/6-31+G(d) frequencies. All reasonable spin states, tautomers, and conformers were evaluated as needed. Thermodynamic quantities assume standard state conditions.

Synthesis of complex [Fe^{II}(*N*-(ethyl-*N*′Me$_2$)(Py)(2-*t*-ButPhOH))(OTf)] (1)

Complex **1** was synthesized in an anaerobic environment inside the glovebox. One equivalent of triethylamine (Et_3N) (75.9 µL, 0.544 mmol) was added to **L1** (186.6 mg, 0.546 mmol) in approximately 5 mL of acetonitrile and reacted for five minutes, followed by the addition of 1.0 equivalents of iron(II) trifluoromethanesulfonate (192.8 mg, 0.545 mmol). The reaction was left to stir for 24 hours at room temperature. The solvent was removed under vacuum, and the resulting residue was washed with diethyl ether (3*x* ∼ 3 mL), resulting in a brown solid after drying. The brown solid was further layered with butanone and diethyl ether (1 : 6 ratio) and left to sit for one hour to yield a green powder (62.6% yield, 186.1 mg, 0.341 mmol). X-ray quality crystals were obtained by the slow vapor diffusion of diethyl ether into butanone, resulting in green crystals.

Elemental analysis for $FeN_3O_4C_{22}H_{30}SF_3$ calcd: C: 47.29%; H: 5.68%; N: 7.88%. Found: C: 46.89%; H: 5.36%; N: 7.34% (Fig. S5). Electronic absorption spectrum (MeCN): λ (nm) (ε (M^{-1} cm^{-1})): 262 (9360 ± 2.29%), 282 (5740 ± 1.35%), 357 (641 ± 3.08%). ESI-MS: image S2.

Synthesis of 3-diazopentane-2,4-dione (substrate precursor)

The substrate precursor was synthesized by modifying the procedure reported by Presset *et al.*[44] Lithium acetylacetone (3.44 g, 32.4 mmol) and potassium carbonate (2.38 g, 17.2 mmol) were mixed with *p*-toluenesulfonyl azide (6.15 g, 31.2 mmol) in 15 mL of acetonitrile and allowed to react for 2.5 hours under constant stirring. After 2.5 hours, stirring was halted and the yellow/orange reaction mixture was filtered through grade 1 Whatman filter paper. The filter was rinsed with dichloromethane (DCM) until the exiting filtrate no longer appeared colored. The solvent was removed under vacuum, yielding crude 3-diazopentane-2,4-dione as a yellow/orange oil. Crude 3-diazopentane-2,4-dione was purified using a Yamazen Smart Flash EPCLC AI-580S chromatography system. The product was twice eluted through silica stationary phase columns with 70 : 30 *n*-hexane/ethyl acetate. Excess solvent was removed under vacuum, yielding pure 3-diazopentane-2,4-dione as a yellow oil (33.6% yield).

Synthesis of 3,3-dihydroxypentan-2,4-dione

Dimethyldioxirane (DMDO) was prepared following published procedures by Taber *et al.* (2014).[45] 3-Diazopentane-2,4-dione (75.6 mg, 0.60 mmol) was dissolved in 1 mL of acetone. DMDO, as a dilute solution in acetone (6 mL), was added to the reaction mixture, and the reaction was allowed to proceed under constant stirring for 1 hour, covered loosely with a rubber septum. After 1 hour, excess solvent and reagents were removed under reduced pressure, yielding colorless crystals of 3,3-dihydroxypentan-2,4-dione (29.5 mg, 0.22 mmol, 37.2% yield). It should be noted that 3,3-dihydroxypentan-2,4-dione is the monohydrate of 2,3,4-pentanetrione; hydration of this triketone occurs readily under atmospheric air.

Oxidative reactivity studies

Reaction of 2-hydroxyacetophenone (2HAPH) with 1 and O_2. For a typical UV-vis experiment, a stock solution of **1** was prepared in acetonitrile (2 mM). A 300 µL aliquot of **1** was added to an anaerobic cuvette with a septum cap inside a glovebox. A stock solution of NEt_3 was also prepared in acetonitrile (72 mM). An aliquot containing 2 mol equivalents of NEt_3, with respect to **1**, was added to the cuvette. A stock solution of 2HAPH was also prepared in acetonitrile. An aliquot containing 20 mol equivalents of 2HAPH, with respect to **1**, was added to the cuvette. Acetonitrile was then added to the cuvette to bring the total reaction volume to 2.2 mL. The reaction cuvette was incubated under anaerobic conditions for 40 minutes to allow for substrate binding. After incubation, 0.5 mol equivalents of O_2 from atmospheric air were injected into the headspace of the cuvette using a gas-tight syringe. Volumetric addition of O_2 was done based on the assumption of the ideal gas law and an atmospheric composition of 21% O_2. The reaction was then monitored for several hours by UV-vis absorption spectroscopy. UV-vis experiments were also conducted at similar concentrations at −40 °C and −80 °C in acetonitrile and acetone, respectively.

For a typical experiment evaluating the oxidation products *via* ^{1}H-NMR, 15 mg. of **1** were dissolved in acetonitrile (4 mL) in a round-bottom flask under anaerobic conditions in a glovebox. An aliquot of 1 mol equivalent 2HAPH and 1 mol equivalent of NEt_3 was added to the flask, and the reaction was anaerobically incubated for 40 minutes. After 40 minutes, an excess of O_2 was bubbled directly into the reaction solution using a needle fitted to tubing attached to a dry oxygen tank for 5 minutes. After 2 hours, the reaction was bubbled for an additional 5 minutes. After 20 hours, the reaction solvent was removed under reduced pressure. The reaction was then quenched with 10% HCl (5 mL), and organic products were extracted with DCM (3 × 10 mL). Solvent was removed under reduced pressure, and the organics were redissolved in $CDCl_3$ for analysis by ^{1}H-NMR.

Reaction of 3-hydroxyflavone (FlaH) with 1 and O_2

For a typical UV-visible experiment, a stock solution of **1** was prepared in dimethylformamide (DMF) (4 mM). A 100 µL aliquot of **1** was added to a vial. A stock solution of FlaH was also prepared in DMF (10 mM). An aliquot of 1 mol equivalent FlaH, with respect to **1**, was also added to the vial; the vial was then diluted to 600 µL with DMF and allowed to incubate under anaerobic conditions for 24 hours. After incubation, a 150 µL aliquot was taken from the vial and transferred to an anaerobic cuvette. DMF was then added to the cuvette to bring the total reaction volume to 2.2 mL. The UV-vis absorption spectrum was then recorded anaerobically, yielding the characteristic spectrum of a bound Fe–FlaH complex.[46] The cuvette was then embedded in a sand bath heated to 50 °C. An excess of O_2 was bubbled directly into the reaction solution using a needle fitted to tubing attached to an oxygen tank for 24 hours. After 24 hours, the cuvette was removed from the heat and active O_2 bubbling. Fresh DMF was added to the cuvette to bring the total solution volume back up to 2.2 mL, and the UV-vis absorption spectrum was recorded.

For a typical ^{1}H-NMR experiment, reaction conditions and workup were identical to those described above in our 2HAPH ^{1}H-NMR experiments with the following exceptions: DMF was used as solvent rather than acetonitrile, the substrate incubation time was 24 hours rather than 40 minutes, oxygenation was continuous for the duration of the reaction, the reaction time was 24 hours rather than 20 hours, and the reaction was carried out in a sand bath heated to 50 °C.

Reaction of 3,3-dihydroxypentan-2,4-dione (3DHPD) with 1 and O_2

For typical UV-visible and ^{1}H-NMR experiments, reaction conditions and workup were identical to those described for our 2HAPH UV-visible and ^{1}H-NMR experiments with the exception of 10 mol equivalents of O_2 being added rather than 0.5 mol equivalents, the reaction time of a ^{1}H-NMR experiment being 24 hours rather than 20 hours, and the workup being done with ethyl acetate rather than DCM.

Results and discussion

Synthesis and characterization of 1

The asymmetric, tripodal N_3O chelating ligand **L1** was synthesized and purified as previously reported.[43] **1** was synthesized and crystallized as described in the experimental procedure in good yields. Crystallographic analysis of complex **1** shows three crystallographically inequivalent 5-coordinate structures in the asymmetric unit, wherein the triflate anions are disordered over two orientations in two of the structures, and the coordinated dimethylamine nitrogen is disordered over two orientations in one of the structures (Fig. S33). This allows for the determination of an average τ value of 0.293. The resultant τ value is generally consistent with complex **1** favoring a square pyramidal over a trigonal bipyramidal coordination geometry.[47] (Fig. 3).

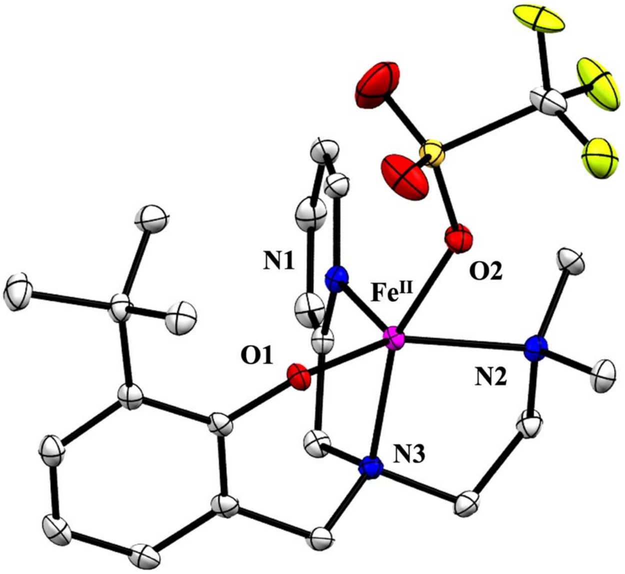

Fig. 3 Representative crystal structure of [Fe(II)(NMe$_2$–6H-Py-2-*t*-ButPhOH)(OTf)] (**1**) with ellipsoids drawn at the 50% probability level. H atoms are omitted from the figure for clarity. Only the primary orientation for disordered sites is shown.

The geometry observed in the crystal structure of model complex **1** is similar to the active site geometries found for Fe-QDO. The crystal structure of Fe-QDO reveals two pentacoordinate iron-containing catalytic domains, one characterized by a distorted trigonal bipyramidal geometry and the other a square pyramid.[48] This pentacoordinate geometry derives from the coordination of the protein-based N_3O motif and an additional aqua moiety.[48] In contrast, a solution structure of human Fe-ARD reveals octahedral geometry derived from the coordination of the N_3O motif and two water moieties.[7]

The average Fe–N1(pyridine) bond length for complex **1** was determined to be 2.11 Å, closely mimicking the Fe–N(His) bond lengths of 2.09 Å determined in the model solution for Fe-ARD (Table 1).[7] This differs significantly from the average Fe–N(His) bond length of 2.22 Å in the crystal structure of Fe-QDO.[48] The average Fe–N2(amine) and Fe–N3(amine) bond lengths for complex **1** were determined to be 2.18 Å and 2.21 Å. These bonds are notably longer than the 2.09 Å Fe–N(His) bond lengths of Fe-ARD; however, they are highly similar to the average Fe–N(His) bond length of 2.22 Å in Fe-QDO.[7,48] The average Fe–O(phenol) bond length for complex **1** was determined to be 1.92 Å; this is shorter than the 2.10 Å Fe–O(Glu) bond in Fe-ARD, and the 2.21 Å and 2.44 Å Fe–O(Glu) bonds at the active sites of Fe-QDO.[7,48] This is expected as the Lewis basicity of the phenolate moiety is higher than that of a carboxylate donor. The average Fe–O(OTf) bond length for complex **1** was determined to be 2.10 Å; this bond length differs from the 1.90 Å Fe–O(water) bond lengths of Fe-ARD, and the average 2.33 Å Fe–O(water) bond length of Fe-QDO.[7,48] In totality, the geometric and structural parameters of complex **1** exhibit reasonable similarity to N_3O coordinate enzymes, suggesting the complex is an effective structural mimic (Table 1).

Table 1 Selected bond lengths in Å for Fe-QDO (close | distant conformations), complex **1**, and Fe-ARD

Fe-QDO		Model complex **1**		Fe-ARD	
Fe–N1 (His)	2.32 | 2.15	Fe–N1	2.11	Fe–N1 (His)	2.09
Fe–N2 (His)	2.16 | 2.23	Fe–N2	2.18	Fe–N2 (His)	2.09
Fe–N3 (His)	2.29 | 2.16	Fe–N3	2.21	Fe–N3 (His)	2.09
Fe–O1 (Glu)	2.10 | 2.44	Fe–O1 (phenol)	1.93	Fe–O1 (Glu)	2.09
Fe–O2 (aqua)	2.21 | 2.44	Fe–O2 (OTf)	2.10	Fe–O2 (aqua)	1.90

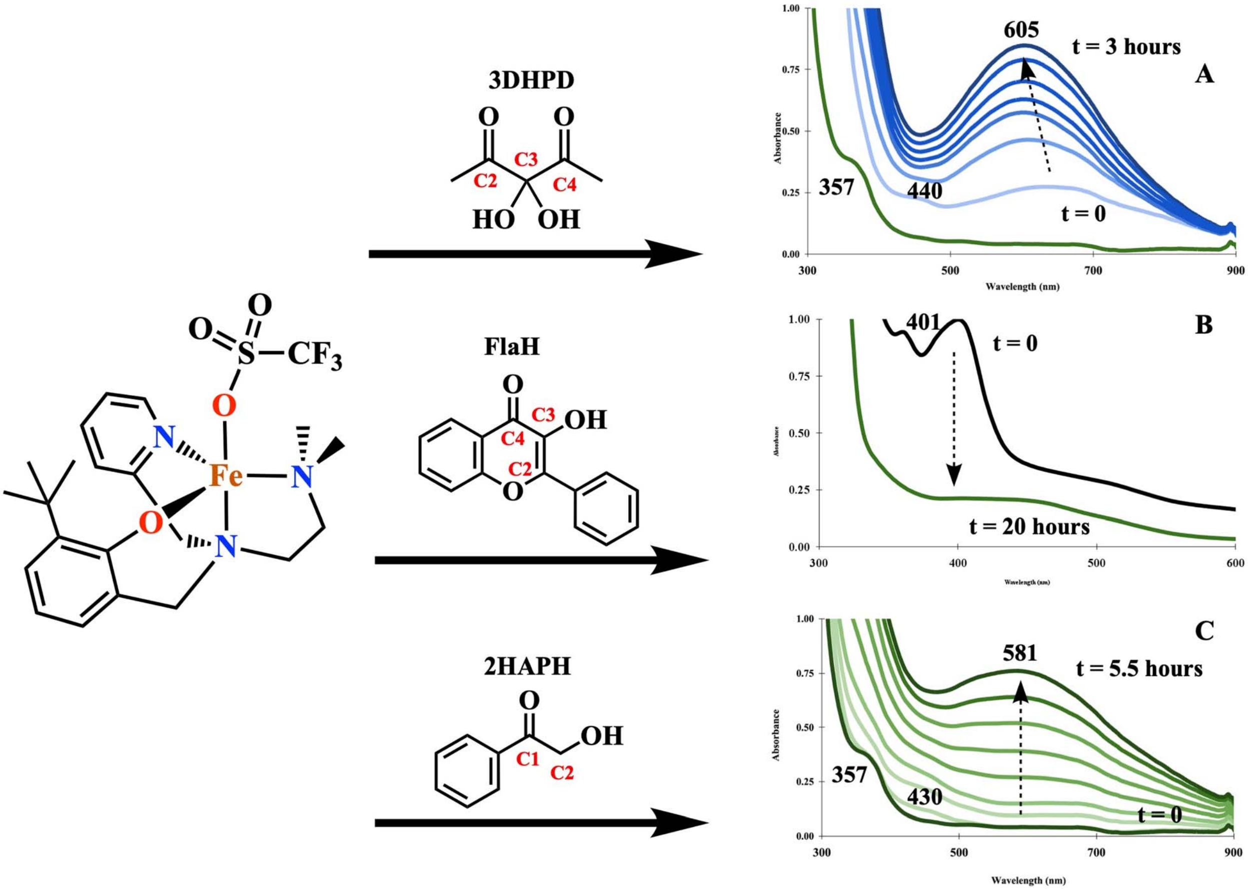

Fig. 4 UV-visible absorption spectrum of the reaction of complex **1** with 3DHPD (A), FlaH (B), and 2HAPH (C) with O_2. For 3DHPD, **1** (0.273 mM) was treated with 20 eq. 3DHPD under 10 eq. O_2 at room temperature in MeCN. For FlaH, **1** (0.045 mM) was treated with 1 eq. FlaH under excess O_2 at 50 °C in DMF. For 2HAPH, **1** (0.273 mM) was treated with 2 eq. NEt_3 and 20 eq. 2HAPH under 0.5 eq. O_2 at room temperature in MeCN. Complete UV-visible absorption data were recorded at 20-minute intervals with the exception of B; these data are available through the SI.

The ^{1}H-NMR spectrum of complex **1** in deuterated methanol (Fig. S1) exhibits paramagnetically shifted signals between 115 and −23 ppm consistent with a Fe(II) $S = 2$ complex. This was confirmed by Evan's method, where we found a magnetic moment (μ_s) = 4.68 BM. This was also confirmed *via* computation (see computational section). The UV-visible absorption spectrum of **1** in acetonitrile displays three absorption bands in the ultraviolet region: $\varepsilon_{262} = 9360\ M^{-1}\ cm^{-1} \pm 2.29\%$, $\varepsilon_{282} = 5740\ M^{-1}\ cm^{-1} \pm 1.35\%$, $\varepsilon_{357} = 641\ M^{-1}\ cm^{-1} \pm 3.08\%$ (Fig. S2). The 357 nm band is consistent with ligand-to-metal charge transfer bands of ferrous model complexes reported in literature, while the intensely absorbing 262 and 282 nm bands may be attributable to ligand-based charge transfer transitions.[23,49,50]

The cyclic voltammogram of complex **1** (1.5 mM) in acetonitrile was obtained using an Ag/$AgNO_3$ reference electrode (10 mM in MeCN) with 0.1 M tetrabutylammonium hexafluorophosphate as supporting electrolyte. All values are reported *vs.* an internal Fc/Fc$^+$ standard. Complex **1** exhibits two peaks in the cyclic voltammogram: $E_{pc} = -15.5$ mV and $E_{pa} = 80.3$ mV (Fig. S3). These peaks are consistent with the assignment of a quasi-reversible Fe^{2+}/Fe^{3+} couple displaying $E_{1/2} = 47.9$ mV ($\Delta E_p = 95.8$ mV), indicating a high degree of accessibility for the Fe(III) state. Outer sphere oxidation of complex **1** using tris(4-bromophenyl)ammoniumyl hexachloroantimonate (magic blue) yields an Fe(III) species with a UV-visible absorption peak maximizing at 665 nm (Fig. S17). The ferric analogue of **1** was synthesized independently (Fig. S18), yielding a consistent UV-visible spectrum.

Biomimetic oxidative C–C bond cleaving reactivity studies

The enzymes ARD, QDO, and DAD are each involved in the carbon–carbon bond cleavage of their respective substrates using O_2 as the oxidant (*vide supra*).[26–28,39,40] To illustrate the versatility in reactivity of model complex **1**, we elected to use 3,3-dihydroxypentan-2,4-dione (3DHPD) as a model substrate of ARD, 3-hydroxyflavone (FlaH) as a model substrate of QDO, and 2-hydroxyacetophenone (2HAPH) as a model substrate of DAD. FlaH and 2HAPH are direct analogs of native QDO and DAD substrates, while 3DHPD is a hydrated triketone analogous in structure to previously reported ARD substrate mimics (Fig. 4).[23]

Incubation for 40 minutes of complex **1** with excess 3DHPD (20 equivalents) under anaerobic conditions in acetonitrile results in the loss of the 357 nm absorption band and the appearance of a broad absorption feature around 440 nm and 650 nm (Fig. 4A). We attribute these changes in the spectrum of **1** to the binding of the protonated 3DHPD. This process is

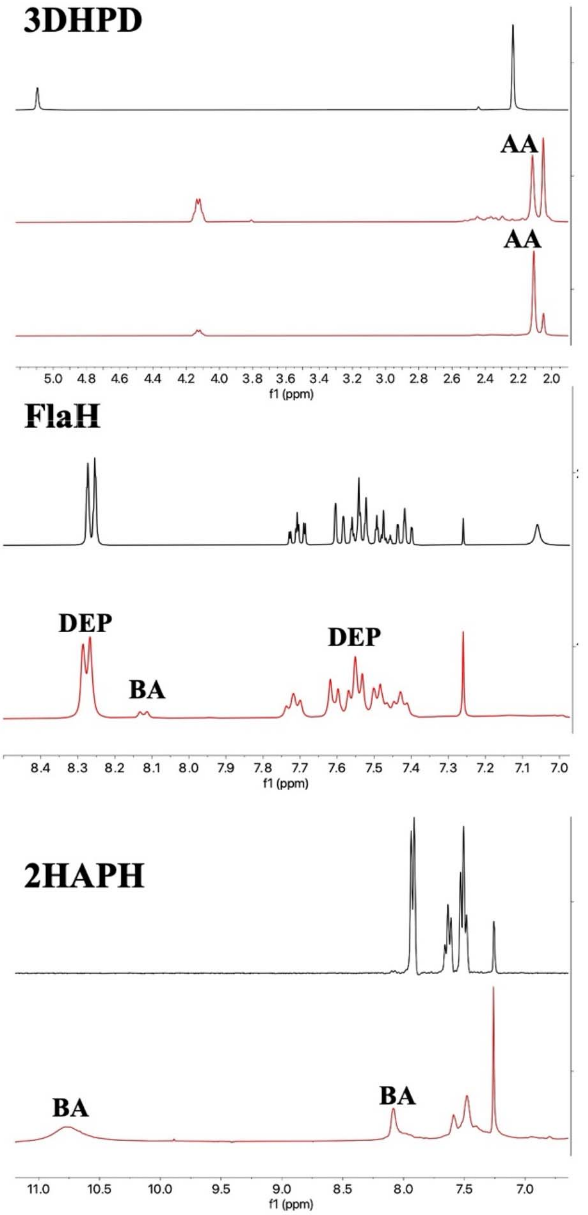

Fig. 5 ^{1}H-NMR in $CDCl_3$ of substrates 3DHPD, FlaH, and 2HAPH (black traces) and their corresponding degradation products upon treatment with complex **1** and O_2 (red traces). 3DHPD trace 2 shows the extracted products of the reaction of **1** with 3 eq. 3DHPD under excess O_2 in acetonitrile corresponding to acetic acid. 3DHPD trace 3 shows the spectrum of extracted products shown in trace 2 after spiking the sample with HOAc, with a growth of the second peak from the right, attributable to acetic acid. FlaH trace 2 shows extracted products of the reaction of **1** with 1 eq. FlaH under excess O_2 in dimethylformamide at 50 °C. 2HAPH trace 2 shows extracted products of the reaction of **1** with 0.25 eq. NEt_3 and 1 eq. 2HAP under excess O_2 in acetonitrile. Abbreviations: AA = acetic acid, DEP = depside (*o*-benzoylsalicylic acid), BA = benzoic acid.

unlikely to be due to a pre-oxidized product since these changes occur under anaerobic conditions. Upon oxygenation (10 equivalents added by gas gas-tight syringe), we observe the growth of an intense 605 nm absorption peak, maximizing after 3 hours (Fig. 4A). This is followed by decay with full loss in definition of the absorption feature over the subsequent ~10 hours (Fig. S5). The dramatic changes observed in the visible spectrum of **1**-3DHPD post-oxygenation are likely attributable to the formation of an intermediate Fe(III) species, consistent with our observations derived from an independently synthesized ferric complex (Fig. S18–S20). The substrate 3DHPD allows for both C2–C3 as well as C3–C4 bond cleavage (Fig. 4A). The cleavage of only the C2–C3 bond would be expected to yield equimolar quantities of acetic acid and pyruvic acid, while cleavage of both C2–C3 and C3–C4 bonds would be expected to yield two equivalents of acetic acid and carbon monoxide. We performed a large-scale reaction of **1**-3DHPD (3 equivalents) under excess O_2 in acetonitrile for 24 hours and evaluated the reaction products by ^{1}H-NMR following organic extraction. The ^{1}H-NMR spectrum of the extracted products reveals the loss of 2.23 ppm and 5.09 ppm signals associated with 3DHPD and the presence of a signal at 2.12 ppm consistent with the methyl protons of acetic acid (Fig. 5-top). This identification is further supported by the growth of the 2.12 ppm signal upon the addition of glacial acetic acid to the reaction products (Fig. 5-top). We performed a qualitative carbon monoxide detection experiment where we observed results consistent with the production of CO (Fig. S6). The observed cleavage of the C2–C3 and C3–C4 bonds of 3DHPD appears analogous to the reaction of 2,3,4-pentanetrione with hydrogen peroxide, in which hydrogen peroxide absent of any metal, mediates the formation of a cyclic intermediate preceding C–C bond cleavage to yield acetic acid and carbon monoxide.[36] The similar nature of this reactivity suggests the reaction of complex **1** with 3DHPD and O_2 may proceed through a similar mechanism by generating H_2O_2, although further mechanistic studies will be required to elucidate this reactivity.

The overnight incubation of complex **1** with FlaH under anaerobic conditions in DMF gives rise to a 401 nm absorption band characteristic of metal-flavone complexes in the literature (Fig. 4B).[33,46] The 401 nm band in the electronic absorption spectrum is attributable to the $\pi \rightarrow \pi^*$ transition of the FlaH substrate coordinated to the metal and differs significantly from the 343 nm λ_{max} of the uncoordinated substrate.[51] A wide range of small-molecule QDO mimics have been presented in literature, ranging from N_3 chelating trispyrazolylborate systems to structurally accurate N_3O systems.[33,52] Unlike the native enzyme, these small molecule systems generally require elevated temperatures for reactivity; most require temperatures from 70–130 °C for flavonoid dioxygenation to occur.[52,53] Upon the treatment of **1**-FlaH with excess O_2 by bubbling directly into DMF solution at 50 °C, we observe the complete loss of the 401 nm absorption feature after 20 hours (Fig. 4B). We attribute the loss of the 401 nm absorption feature to C2–C3 and C3–C4 bond cleavage in the central ring of FlaH-(Fig. 4B). Oxygenation of the substrate under identical conditions does not result in substrate decomposition (Fig. S7). We performed a large-scale reaction of **1**-FlaH (1 equivalent) under the same conditions and evaluated the reaction products by ^{1}H-NMR following organic extraction. The ^{1}H-NMR spectrum of the extracted products shows production of a depside product, *ortho*-benzoylsalicylic acid, in 88% yield. Additionally, we detect qualitatively the formation of carbon monoxide (Fig. S8). This product has been reported in the QueD literature as a result of the oxidative C–C cleavage of FlaH (Fig. 5-middle).[33,53] The oxygen-mediated degradation of FlaH by complex **1** at 50 °C indicates that complex **1** compares favorably to existing QDO model systems requiring elevated temperatures. Sun *et al.* have previously reported a set of N_3O coordinate QDO mimics in which they attribute lower temperature catalytic activity to the increased electron-donating ability of a carboxylate oxygen donor to the metal center.[46] Similarly, **L1** has an even stronger donating phenolate oxygen. Further mechanistic studies are underway in our laboratory alongside selective modifications to ligand **L1** to understand the drivers of this reactivity.

Incubation of complex **1** with excess 2HAPH (20 equivalents) and triethylamine (2 equivalents) under anaerobic conditions for 40 minutes in acetonitrile results in the deformation of the 357 nm absorption band, and the appearance of a 430 nm shoulder (Fig. 4C). We attribute this deformation in the spectrum of **1** to the ferrous metal center binding 2HAP. This binding event is also observed by ^{1}H-NMR, wherein significant changes in the paramagnetic region are observed upon the addition of 2HAPH to complex **1** (Fig. S10). Upon oxygenation (0.5 equivalents added by gas-tight syringe), we observe the growth of an intense, broad 581 nm absorption peak, maximizing 6.5 hours post-oxygenation (Fig. 4C). This is followed by decay with gradual loss in the definition and intensity of the absorption feature over the subsequent several days; 72 hours post-oxygenation, the 581 nm band remained observable at 72% of maximum absorption intensity (Fig. S13). We attribute the stability of this absorption feature in part to the formation of stable ferric-benzoate species, resulting from the C1–C2 oxidative cleavage of the substrate (Fig. 4C), analogous to the reactivity of native DAD. This band compares well with the independent addition of benzoate to the ferric analogue of **1** (Fig. S19).

We performed a large-scale reaction of **1**-2HAP wherein 2HAPH (1 equivalent) and triethylamine (0.25 equivalent) were incubated for 40 minutes under anaerobic conditions in acetonitrile. The acetonitrile solution was then oxygenated (excess O_2 bubbled into the reaction from a dry oxygen tank for 5 minutes) and allowed to react for 20 hours, after which time the organic reaction products were extracted and analyzed by ^{1}H-NMR. The ^{1}H-NMR spectrum of the extracted products shows no presence of signals associated with the 2HAPH substrate in the aromatic region (7.94 ppm, 7.64 ppm, 7.51 ppm) (Fig. 5-bottom). Rather, we observe signals corresponding to benzoic acid (8.09 ppm, 7.59 ppm, 7.48 ppm). A broad downfield 10.8 ppm signal is also observed, which we also attribute to benzoic acid. This comports with similar changes in the NMR spectra when an analogous reaction is run *in situ* in MeOD (Fig. S11). Quantitative analysis of the NMR experiment suggests a yield of 66% of benzoic acid (Fig. S16). The reaction with 2HAPH was also performed at low temperatures (−40 °C in acetonitrile and −80 °C in acetone), to observe any transient species during the reactivity. During the growth process, we observe very broad absorptions in the range of 450–700 nm that sharpen over time (Fig. S14 and S15). This broadness could suggest intermediates that can't be discerned under the conditions we ran the reaction.

We note that the products of the aforementioned biomimetic reactions are distinct from the reaction of **1** with O_2, absent any substrate. Unlike native enzymatic systems, small model iron complexes are susceptible to O_2 mediated dimerization reactions.[54] In the absence of a biomimetic substrate, we observe significant changes in the electron absorption spectrum of complex **1** upon reactivity with excess O_2, with the growth of an intense 551 nm attributed to the dimerization product, a ferric μ-oxo dimer (Fig. S18). This purple species is indefinitely stable under air and hygroscopic. Formation of this species is supported by DFT calculations, suggesting that the μ-oxo is thermodynamically accessible (*vide infra*). This identity was confirmed crystallographically, consistent with our assignment (Fig. S22).

Computational analysis for the proposed mechanism of the O_2 mediated oxidation of 2-hydroxyacetophenone (2HAPH) by 1

DFT calculations used levels of theory akin to those used by Chavez *et al.* and ourselves in recent studies of related iron-DAD and nickel-ARD biomimetics, respectively.[43,50] Particular attention was focused on the early steps in the reaction scheme, given the growing interest in biomimetic oxidation by Earth-abundant 3d metals using dioxygen and the fact that the C–C cleavage and subsequent steps are computed to be highly exergonic. A summary of the proposed mechanism is shown in Fig. 9.

The energetics of 2-hydroxyacetophenone (2HAPH) deprotonation in SMD continuum acetonitrile solvent were calculated. The free energy to displace triflate by 2HAPH is exergonic by 2.7 kcal mol^{-1}, Fig. S29. Using triethylamine (NEt_3) as a model base, $\Delta G_{\text{deprot.}}$ is computed to be +21.3 kcal mol^{-1} to remove the hydroxyl proton of the 2HAPH ligand. Upon coordination of 2HAPH, $\Delta G_{\text{deprot.}}$ by NEt_3 is reduced by ∼11 kcal mol^{-1} to +7.9 kcal mol^{-1}. This calculated acidification corresponds to a decrease of ∼9 pK_a units. Coordination of the neutral substrate – κ^2-O,O′– to the iron(II) thus greatly enhances its acidity. The Mulliken atomic charge on the hydroxyl proton is +0.37 *vs.* +0.31 e^- for free 2-hydroxyacetophenone at the same level of theory. The charges thus infer that enhanced acidity of the metal-bound substrate arises from stabilization of the anionic ligand upon deprotonation as well as enhanced Brønsted–Lowry acidity of the hydroxyl proton arising from σ-donation to the central metal ion.

The DFT calculations also suggest that coordination of the substrate to the iron(II) center makes it easier to oxidize relative to the Fe(II)-OTf bound starting material (**1**). To model an outer-sphere electron transfer (ET) pathway, the free energy of electron transfer to O_2 to make superoxide was computed. For the neutral Fe^{II}-OTf (**1**) starting material, ΔG_{ET} = +29.9 kcal mol^{-1} to form superoxide and the cationic Fe(III) triflate complex. For the neutral Fe^{II}-2HAP complex, the corresponding ET reaction to make superoxide is greatly reduced, ΔG_{ET} = +9.7 kcal mol^{-1}. Upon oxidation, the coordination geometry of the Fe^{II}-2HAP

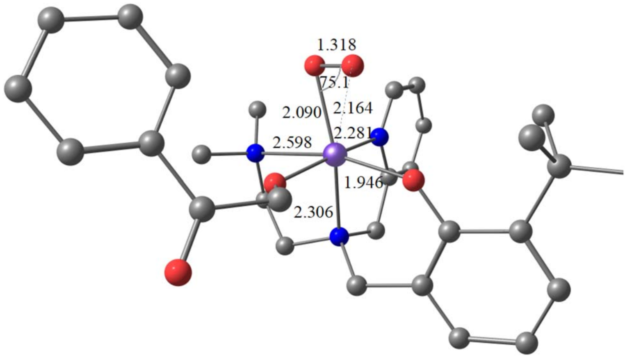

Fig. 6 DFT optimized geometry of a Fe^{III}-superoxide complex. Bond lengths in Angstrom units and bond angles in degrees.

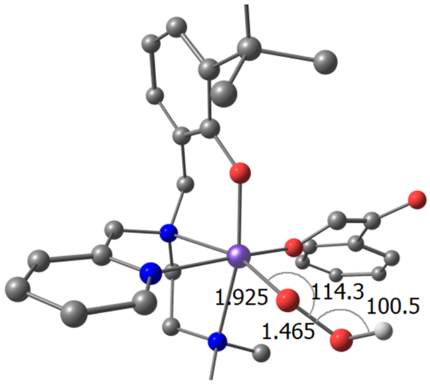

Fig. 8 Fe–OOH intermediate. Bond lengths are in Angstrom units; bond angles in degrees.

complex changes moderately, with the expected contraction of Fe-ligand distances (~0.08 Å on average) and variation of metal-dependent bond angles by 3.8°. Comparing the HOMO (highest occupied Kohn–Sham molecular orbital) energies for Fe^{II}-OTf (−5.06 eV) and Fe^{II}-2HAP (−4.37 eV) indicates the latter orbital energy is higher, consistent with the latter being more easily oxidized.

An inner-sphere oxidation pathway was also considered, and the free energy for O_2 coordination was computed to be mildly endergonic, $\Delta G = +3.4$ kcal mol^{-1}. In coordinating with the Fe, the O_2 displaces the carbonyl arm of the erstwhile κ^2-O,O′-2HAP. The optimized OO bond length is 1.318 Å (Fig. 6), which compares with 1.351 and 1.215 Å for free superoxide anion and triplet dioxygen, respectively, at the same level of theory. Additionally, the minimized structure displays a significant lengthening of the Fe–N2 (–NMe_2) bond to 2.598 Å. This change allows for the distal oxygen on the OO moiety to achieve a bonding length of 2.164 Å, akin to a side-on OO adduct. The electronic structure of the Fe-2HAP-O_2 adduct is particularly interesting, showing ~1.3 e^- of total spin density on the two oxygen atoms of the O_2 ligand, with slightly more on the terminal oxygen; the remaining spin density resides on the complex, largely situated on the iron with a modest amount of spin density on the ligating atoms of the N_3O supporting ligand and the ligating oxygen of the deprotonated 2HAP ligand (Fig. S30). Considering the calculated spin density and OO bond lengths, this complex is viewed primarily as an Fe^{III}-superoxide with an admixture of Fe^{II}-dioxygen character.

For the Fe^{III}-superoxide, there is a transition state (Fig. 7, left) with a modest barrier to C–H activate a C_α-H bond of the 2HAP substrate by the coordinated superoxide, $\Delta G^{\#} = 12.2$ kcal mol^{-1}, leading to an Fe^{III}-hydroperoxide. The H-atom transfer process is computed to be exergonic, $\Delta G_{HAT} = -10.3$ kcal mol^{-1}. An isomeric outer-sphere C_α–H bond activation TS (Fig. 7, right) was also isolated and computed to be 5.6 kcal mol^{-1} higher than the inner sphere TS just mentioned. The computations thus suggest a kinetic advantage for an inner-sphere oxidation pathway.

Calculations suggest that the Fe–OOH intermediate formed by inner-sphere C–H activation (Fig. 8) is deprotonated with relative ease, again using NEt_3 as a model base, $\Delta G = +14.8$ kcal mol^{-1}, respectively. Hence, we propose that after the HAT step to make Fe–OOH (HS Fe(II)), this complex is deprotonated to give anionic $FeOO^-$which undergoes a barrierless nucleophilic attack of the OO ligand to the carbonyl carbon to make a dioxetane intermediate, $\Delta G = -5.5$ kcal mol^{-1}. We were unable to isolate the TS for decomposition of the dioxetane intermediate, but this reaction is extremely exergonic, $\Delta G = -116.8$ kcal mol^{-1}, and is computed to favor the observed products, *i.e.*, Fe^{II}-

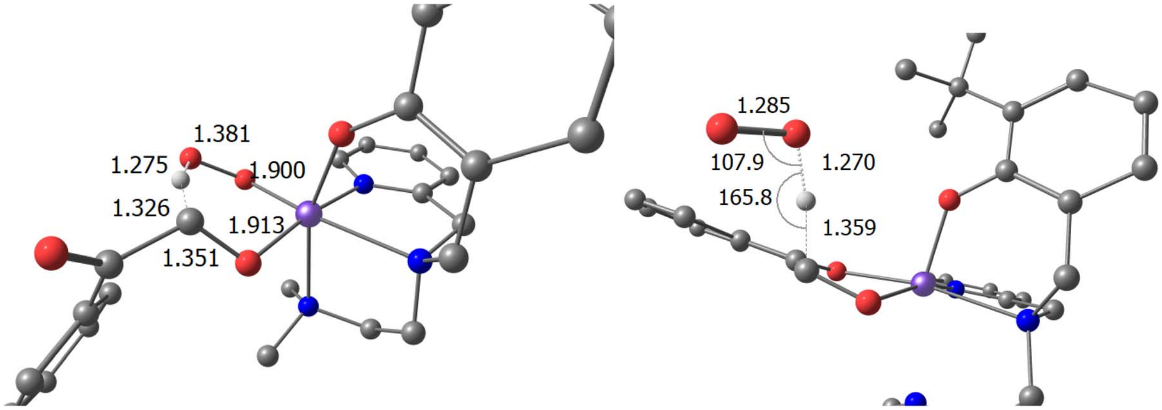

Fig. 7 Comparison of inner (left) and outer (right) sphere transition states for C–H activation of the alpha carbon of the iron-ligated 2HAP ligand. Bond lengths in Angstrom units.

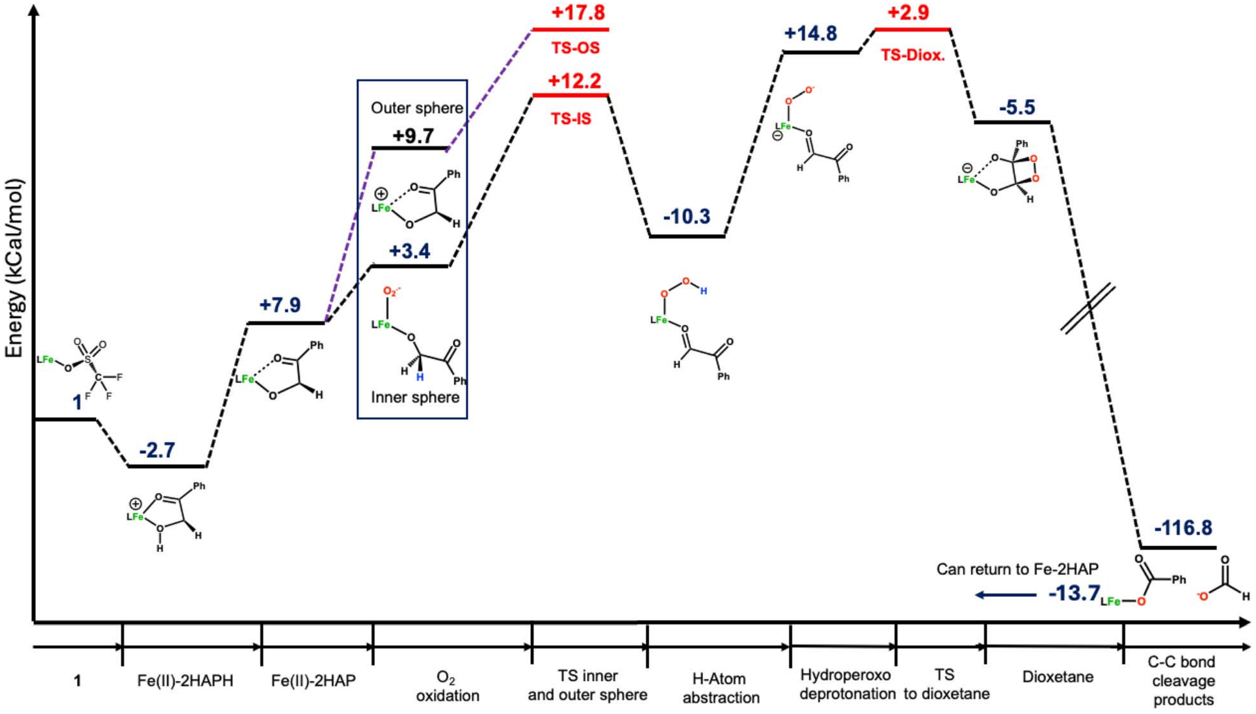

Fig. 9 Summary of the proposed reaction mechanism for the O_2-mediated C–C bond cleavage of 2HAPH by **1**.

benzoate + formate anion by ∼3 kcal mol^{-1} relative to the alternative formulation of Fe^{II}-formate + benzoate anion. Displacement of the benzoate ligand by the conjugate base of 2HAPH to initiate another round of catalysis is calculated to be exergonic by −13.7 kcal mol^{-1}.

Of note is the lengthening of the Fe(II)–NMe_2 bond length, both during the binding of deprotonated 2HAP and more significantly during the Fe–O_2-substrate adduct formation, 2.373 Å (Fig. S31) and 2.598 Å (Fig. 6), respectively. For both complexes, we found computationally three linkage isomers within 3 kcal mol^{-1} of each other, with the lowest energy favoring the loosely bound amine moiety. While this energy difference is not conclusive of the preference of one isomer over another, we argue that the ability of the unbound N_2O isomer to exist is suggestive of potentially relevant geometrical flexibility, which was not observed for the Ni(II) counterpart.[43] Miłaczewska *et al.* reported in 2018 a finding of histidine dissociation in iron-containing ARD by EPR, with their computational and spectroscopic evidence pointing to the dissociation of His 88. They reported that only Fe-ARD demonstrated an ability to dissociate one of the histidine residues during ARD oxidation.[35]

As noted earlier, the parent Fe(II)-OTf complex (**1**) reacts readily with excess O_2 at ambient conditions to form an Fe(III)–O–Fe(III) dimer (Fig. S22).[54–56] We explored this reactivity *via* DFT calculations (Fig. S32). This product could be accessed *via* an inner sphere O_2 oxidation of an Fe(II)-OTf (**1**) to form a monomeric Fe(III)-superoxo ($\Delta G = 10.9$ kcal mol^{-1}). Subsequently, it can be further oxidized by another equivalent of Fe(II)-OTf to form Fe(III)–OO–Fe(III) (μ-peroxo dimer, $\Delta G = 1.8$ kcal mol^{-1}). This μ-peroxo complex decomposes in an exergonic fashion to two Fe(IV)═O complexes ($\Delta G = -4.3$ kcal mol^{-1}), which then combine with additional Fe(II)-OTf (**1**) to yield the proposed Fe(III)-μ-oxo dimer ($\Delta G = 0.56$ kcal mol^{-1}). A similar mechanism has been proposed previously for the formation of these dimers.[54] The possible formation of a transient Fe(IV)═O complex (Fig. S32) is intriguing for the tetrad N_3O geometry, given that this intermediate is the canonical high-valent oxidant invoked for N_2O triad iron oxygenases. In preliminary studies, we performed low-temperature reactivity UV-visible studies for complex **1** with the oxygen atom donor *meta*-chloroperbenzoic acid (mCPBA) and O_2 (Fig. S23–S27). The reaction of **1** with mCPBA (1 eq.) in acetonitrile at −40 °C results in the growth of a band at 620 nm, presumably the result of a one-electron oxidation of the starting material to a ferric-chlorobenzoate species. This persists upon warming to room temperature (Fig. S23). Precedent for mCPBA acting as a one-electron oxidant has been previously reported.[57] When the same reaction is run at colder temperatures in acetone (−80 °C) with 6 eq. of mCPBA, we observe the growth of a similar UV-visible feature at 620 nm (Fig. S24A). Over the course of 6 minutes, this intermediate cleanly transitions to a new intermediate with a rise of a prominent absorption features at 434 nm, 474 nm both of which decay upon warming to room temperature (Fig. S24-B and C). These features are similar to literature reports of Fe(IV)═O complexes.[58] These compounds exhibit an additional band around 700–800 nm, although with extinction coefficients one to two orders of magnitude below that of the 400–500 nm characteristic bands. We observe only a broad shoulder in this region.

In an attempt to observe an intermediate during the reaction of **1** with O_2, we ran this reaction at − 40 and − 80 °C in acetonitrile and acetone, respectively (Fig. S25–S27). We observe general broadening during the growth of the μ-oxo dimer absorption feature; however, no clear intermediates were observed. While these experiments don't yield conclusive evidence of a particular intermediate proposed in the DFT calculations of the ferric-μ-oxo dimer, the potential ability to access the high-valent state in an N_3O coordination environment is intriguing and relevant to our argument that this more unusual active site coordination could be flexible enough to access similar intermediates, *i.e.*, Fe(III)-superoxo and Fe(IV)=O, as those accessible for the N_2O triad.

Summary and conclusions

We report the synthesis and characterization of a novel structural and functional model of N_3O coordinate C–C bond cleaving dioxygenase enzymes QDO and ARD. Complex **1** displays versatile dioxygenase-like C–C bond cleavage reactivity in the biomimetic substrates 3-hydroxyflavone, 2-hydroxyacetophenone, and 3,3-dihydroxypentan-2,4-dione. This reactivity was studied *via* ^{1}H-NMR, UV-vis, and DFT studies. A computationally derived reaction mechanism for the side chain C–C bond cleavage of 2-hydroxyacetophenone points to direct O_2 activation at the metal, leading to a putative Fe(III)-superoxo as the oxidant. **1** can activate O_2, leading to the formation of a ferric-μ-oxo dimer. Low-temperature UV-visible studies implicate the presence of intermediates, suggesting the formation of high-valent Fe species, mirroring those observed in mimics of the N_2O coordinate enzymes. The ferric analogue of **1** is accessible under mild oxidative conditions, *e.g.*, outer sphere oxidants and O_2, adding further evidence to the possibility that a redox process is relevant to the oxidative carbon cleavage in ARD and other dioxygenases with an N_3O coordinating motif. Our computational work supports previous observations in the ARD literature, suggesting the presence of transient shifts in the coordination mode of the iron center from N_3O tetrad to N_2O triad during the oxidation mechanism. The versatility of reactivity observed in this complex points to the unique characteristics afforded by the atypical N_3O coordination motif. This reactivity challenges the canonical understanding of N_3O coordinate iron systems and may have implications for the reaction mechanisms of enzymes, including ARD and QDO. Given that most functional models of non-heme dioxygenase enzymes employ N_3 or N_4 coordinate systems bearing pyrazole, pyridine, and alkyl amine donors,[10,23,49,52,59] it is easy to overlook the contributions of the actual coordination motif to a particular mechanism. We suggest there is a benefit of further exploring operable mechanisms in both the 2-His-1-carboxylate triad and the less common 3-His-1-carboxylate tetrad, and that further biomimetic study using structurally relevant complexes such as **1** could prove valuable in probing the contributions of atypical coordination to the enzymatic mechanisms of ARD, QDO, and other underexplored oxidative chemistry.

Author contributions

Conceptualization: Fadul, Toledo; data curation: Fadul, Toledo; formal analysis: Fadul, Toledo; funding acquisition: Toledo, Cundari, Bertke; investigation: Fadul, Toledo, Cundari, Bertke; methodology: Fadul, Toledo, Cundari, Bertke; project administration: Fadul, Toledo; resources: Toledo, Cundari, Bertke; software: Cundari, Bertke; supervision: Toledo; validation: Fadul, Toledo, Cundari, Bertke; visualization: Fadul, Toledo, Cundari, Bertke; writing-original draft: Fadul; writing-review & editing: Fadul, Toledo, Cundari, Bertke.

Conflicts of interest

There are no conflicts to declare.

Data availability

Additional data files, including complete UV-visible, CV, NMR, crystallography, and computational files used for this manuscript, are available at the American University Research Archive (AURA) at DOI: https://doi.org/10.57912/c.8040217.

CCDC 2486757 (**1**) and 2515966 contain the supplementary crystallographic data for this paper.[60a,b]

The data supporting this article have been included as part of the supplementary information (SI). Supplementary information. See DOI: https://doi.org/10.1039/d5ra09716a

Acknowledgements

S. T. acknowledges American University College of Arts and Sciences Faculty start-up fund, College of Arts & Sciences Summer Undergraduate Fellowship, and the Chemistry Department at American University for student stipend support. National Institute of General Medical Sciences of the National Institutes of Health under Award Number SC2GM130438 for partial financial support. The content is solely the responsibility of the authors and does not necessarily represent the official views of the National Institutes of Health. This work was supported in part by the National Science Foundation (CHE-2202693) through the NSF Center for Computer-Assisted Synthesis (C-CAS). Supplies and funding for a summer research fellowship student (SURF) were provided by CCAS. For initial contributions to the ferric chemistry, we acknowledge the CCAS-SURF student Aidan Durant. T. R. C. acknowledges the U.S. Department of Energy, Office of Science, Office of Basic Energy Sciences, Chemical Sciences Division, Catalysis Science Program, for partial support of this research through grant DE-FG02-03ER15387. We also gratefully acknowledge NSF support for the UNT CASCaM HPC cluster *via* grants CHE-1531468 and OAC-2117247. We recognize Dr Yue Li and the Mass Spectrometry facility in the Department of Chemistry and Biochemistry at the University of Maryland–College Park for use of the Bruker Maxis-II Q-TOF mass spectrometer (Purchase of the Bruker Maxis-II was supported by Award Number-2018860 from the National Science Foundation).

Notes and references

1 O. Hayaishi, Oxygenases, in *Encyclopedia of Biological Chemistry*, ed. Lennarz W. J. and Lane M. D., Academic Press, Waltham, 2nd edn, 2013, pp. , pp. 371–374, https://

www.sciencedirect.com/science/article/pii/B9780123786302001274.

2 S. Lancellotti, L. Novarese and R. De Cristofaro, Biochemical Properties of Indoleamine 2,3-dioxygenase: From Structure to Optimized Design of Inhibitors, *Curr. Med. Chem.*, 2011, **18**(15), 2205–2214.

3 S. C. Daubner, T. Le and S. Wang, Tyrosine hydroxylase and regulation of dopamine synthesis, *Arch. Biochem. Biophys.*, 2011, **508**(1), 1–12.

4 J. Druker, J. W. Wilson, F. Child, D. Shakir, T. Fasanya and S. Rocha, Role of Hypoxia in the Control of the Cell Cycle, *Int. J. Mol. Sci.*, 2021, **22**(9), 4874.

5 N. R. Lee, D. Y. Kwon and K. H. Min, Cloning and sequence analyses of a 2,3-dihydroxybiphenyl 1,2-dioxygenase gene (bphC) from Comamonas sp. SMN4 for phylogenetic and structural analysis, *J. Ind. Microbiol. Biotechnol.*, 2003, **30**(4), 245–250.

6 A. R. Deshpande, T. C. Pochapsky and D. Ringe, The Metal Drives the Chemistry: Dual Functions of Acireductone Dioxygenase, *Chem. Rev.*, 2017, **117**(15), 10474–10501.

7 X. Liu, A. Garber, J. Ryan, A. Deshpande, D. Ringe and T. C. Pochapsky, A Model for the Solution Structure of Human Fe(II)-Bound Acireductone Dioxygenase and Interactions with the Regulatory Domain of Matrix Metalloproteinase I (MMP-I), *Biochemistry*, 2020, **59**(44), 4238–4249.

8 M. E. Runda, N. A. W. de Kok and S. Schmidt, Rieske Oxygenases and Other Ferredoxin-Dependent Enzymes: Electron Transfer Principles and Catalytic Capabilities, *ChemBioChem*, 2023, **24**(15), e202300078.

9 M. M. Mbughuni and J. D. Lipscomb, Iron Proteins, Mononuclear (non-heme) Iron Oxygenases, in *Encyclopedia of Metalloproteins*, ed. Kretsinger R. H., Uversky V. N. and Permyakov E. A., Springer, New York, NY, 2013, pp. 1006–1015, DOI: 10.1007/978-1-4614-1533-6_357.

10 M. Costas, M. P. Mehn, M. P. Jensen and L. Que, Dioxygen Activation at Mononuclear Nonheme Iron Active Sites: Enzymes, Models, and Intermediates, *Chem. Rev.*, 2004, **104**(2), 939–986.

11 E. L. Hegg and L. Q. Jr, The 2-His-1-Carboxylate Facial Triad — An Emerging Structural Motif in Mononuclear Non-Heme Iron(II) Enzymes, *Eur. J. Biochem.*, 1997, **250**(3), 625–629.

12 S. Kal and L. Que, Dioxygen activation by nonheme iron enzymes with the 2-His-1-carboxylate facial triad that generate high-valent oxoiron oxidants, *JBIC, J. Biol. Inorg. Chem.*, 2017, **22**(2), 339–365.

13 L. D. Eltis, B. Hofmann, H. J. Hecht, H. Lünsdorf and K. N. Timmis, Purification and crystallization of 2,3-dihydroxybiphenyl 1,2-dioxygenase, *J. Biol. Chem.*, 1993, **268**(4), 2727–2732.

14 Y. Uragami, T. Senda, K. Sugimoto, N. Sato, V. Nagarajan, E. Masai, *et al.*, Crystal structures of substrate free and complex forms of reactivated BphC, an extradiol type ring-cleavage dioxygenase, *J. Inorg. Biochem.*, 2001, **83**(4), 269–279.

15 T. A. Dix, D. M. Kuhn and S. J. Benkovic, Mechanism of oxygen activation by tyrosine hydroxylase, *Biochemistry*, 1987, **26**(12), 3354–3361.

16 K. M. Roberts and P. F. Fitzpatrick, Mechanisms of Tryptophan and Tyrosine Hydroxylase, *IUBMB Life*, 2013, **65**(4), 350–357.

17 M. S. Lah, M. M. Dixon, K. A. Pattridge, W. C. Stallings, J. A. Fee and M. L. Ludwig, Structure-function in Escherichia coli iron superoxide dismutase: comparisons with the manganese enzyme from Thermus thermophilus, *Biochemistry*, 1995, **34**(5), 1646–1660.

18 E. Yikilmaz, J. Porta, L. E. Grove, A. Vahedi-Faridi, Y. Bronshteyn, T. C. Brunold, *et al.*, How Can a Single Second Sphere Amino Acid Substitution Cause Reduction Midpoint Potential Changes of Hundreds of Millivolts?, *J. Am. Chem. Soc.*, 2007, **129**(32), 9927–9940.

19 W. Minor, J. Steczko, B. Stec, Z. Otwinowski, J. T. Bolin, R. Walter, *et al.*, Crystal Structure of Soybean Lipoxygenase L-1 at 1.4 Å Resolution, *Biochemistry*, 1996, **35**(33), 10687–10701.

20 M. H. Glickman and J. P. Klinman, Lipoxygenase Reaction Mechanism: Demonstration That Hydrogen Abstraction from Substrate Precedes Dioxygen Binding during Catalytic Turnover, *Biochemistry*, 1996, **35**(39), 12882–12892.

21 C. E. Valdez, N. M. Gallup and A. N. Alexandrova, Co^{2+} acireductone dioxygenase: Fe2+ mechanism, Ni2+ mechanism, or something else?, *Chem. Phys. Lett.*, 2014, **604**, 77–82.

22 G. A. Blade, R. Parveen, J. L. Jaimes, W. Ilustre, D. Saldaña, D. A. Ivan, *et al.*, A family of structural and functional models for the active site of a unique dioxygenase: Acireductone dioxygenase (ARD), *J. Inorg. Biochem.*, 2020, **212**, 111253.

23 C. J. Allpress, K. Grubel, E. Szajna-Fuller, A. M. Arif and L. M. Berreau, Regioselective Aliphatic Carbon–Carbon Bond Cleavage by a Model System of Relevance to Iron-Containing Acireductone Dioxygenase, *J. Am. Chem. Soc.*, 2013, **135**(2), 659–668.

24 C. J. Allpress and L. M. Berreau, A Nickel-Containing Model System of Acireductone Dioxygenases that Utilizes a C(1)–H Acireductone Substrate, *Eur. J. Inorg. Chem.*, 2014, **27**, 4642–4649.

25 D. Jeong, S. Sun, D. Moon and J. Cho, A functional model for quercetin 2,4-dioxygenase: Geometric and electronic structures and reactivity of a nickel(II) flavonolate complex, *J. Inorg. Biochem.*, 2022, **226**, 111632.

26 S. C. Chai, T. Ju, M. Dang, R. B. Goldsmith, M. J. Maroney and T. C. Pochapsky, Characterization of Metal Binding in the Active Sites of Acireductone Dioxygenase Isoforms from Klebsiella ATCC 8724, *Biochemistry*, 2008, **47**(8), 2428–2438.

27 A. R. Deshpande, K. Wagenpfeil, T. C. Pochapsky, G. A. Petsko and D. Ringe, Metal-Dependent Function of a Mammalian Acireductone Dioxygenase, *Biochemistry*, 2016, **55**(9), 1398–1407.

28 I. M. Kooter, R. A. Steiner, B. W. Dijkstra, P. I. van Noort, M. R. Egmond and M. Huber, EPR characterization of the mononuclear Cu-containing Aspergillus japonicus quercetin 2,3-dioxygenase reveals dramatic changes upon

anaerobic binding of substrates, *Eur. J. Biochem.*, 2002, **269**(12), 2971–2979.

29 R. A. Steiner, K. H. Kalk and B. W. Dijkstra, Anaerobic enzyme substrate structures provide insight into the reaction mechanism of the copper-dependent quercetin 2,3-dioxygenase, *Proc. Natl. Acad. Sci. U. S. A.*, 2002, **99**(26), 16625–16630.

30 L. Bowater, S. A. Fairhurst, V. J. Just and S. Bornemann, *Bacillus subtilis* YxaG is a novel Fe-containing quercetin 2,3-dioxygenase, *FEBS Lett.*, 2004, **557**(1–3), 45–48.

31 D. Nianios, S. Thierbach, L. Steimer, P. Lulchev, D. Klostermeier and S. Fetzner, Nickel quercetinase, a "promiscuous" metalloenzyme: metal incorporation and metal ligand substitution studies, *BMC Biochem.*, 2015, **16**(1), 10.

32 X. Yan, H. Xiao, J. Song and C. Li, Unraveling the Pivotal Roles of Various Metal Ion Centers in the Catalysis of Quercetin 2,4-Dioxygenases, *Molecules*, 2023, **28**(17), 6238.

33 Y. J. Sun, Q. Q. Huang, T. Tano and S. Itoh, Flavonolate Complexes of MII (M = Mn, Fe, Co, Ni, Cu, and Zn). Structural and Functional Models for the ES (Enzyme–Substrate) Complex of Quercetin 2,3-Dioxygenase, *Inorg. Chem.*, 2013, **52**(19), 10936–10948.

34 J. H. Jeoung, D. Nianios, S. Fetzner and H. Dobbek, Quercetin 2,4-Dioxygenase Activates Dioxygen in a Side-On O2–Ni Complex, *Angew. Chem., Int. Ed.*, 2016, **55**(10), 3281–3284.

35 A. Miłaczewska, E. Kot, J. A. Amaya, T. M. Makris, M. Zając, J. Korecki, *et al.*, On the Structure and Reaction Mechanism of Human Acireductone Dioxygenase, *Chem.–Eur. J.*, 2018, **24**(20), 5225–5237.

36 Y. Dai, T. C. Pochapsky and R. H. Abeles, Mechanistic Studies of Two Dioxygenases in the Methionine Salvage Pathway of *Klebsiella pneumoniae*, *Biochemistry*, 2001, **40**(21), 6379–6387.

37 M. Sparta, C. E. Valdez and A. N. Alexandrova, Metal-Dependent Activity of Fe and Ni Acireductone Dioxygenases: How Two Electrons Reroute the Catalytic Pathway, *J. Mol. Biol.*, 2013, **425**(16), 3007–3018.

38 Y. J. Sun, Q. Q. Huang and J. J. Zhang, Series of Structural and Functional Models for the ES (Enzyme–Substrate) Complex of the Co(II)-Containing Quercetin 2,3-Dioxygenase, *Inorg. Chem.*, 2014, **53**(6), 2932–2942.

39 D. J. Hopper, Oxygenase properties of the (4-hydroxybenzoyl) methanol-cleavage enzyme from an Alcaligenes sp, *Biochem. J.*, 1986, **239**(2), 469–472.

40 R. Keegan, A. Lebedev, P. Erskine, J. Guo, S. P. Wood, D. J. Hopper, *et al.*, Structure of the 2,4′-dihydroxyacetophenone dioxygenase from Alcaligenes sp. 4HAP, *Acta Crystallogr. D*, 2014, **70**(9), 2444–2454.

41 The Evans Method, *Calculating Unpaired Electrons and Magnetic Susceptibility*, https://app.jove.com/v/10304/the-evans-method-calculating-unpaired-electrons-magnetic.

42 D. A. Levaggi and M. Feldstein, The Colorimetric Determination of Low Concentrations of Carbon Monoxide, *Am. Ind. Hyg. Assoc. J.*, 1964, **25**(1), 64–66.

43 K. E. Kirsch, M. E. Little, T. R. Cundari, E. El-Shaer, G. Barone, V. M. Lynch, *et al.*, Direct O2 mediated oxidation of a Ni(II)N3O structural model complex for the active site of nickel acireductone dioxygenase (Ni-ARD): characterization, biomimetic reactivity, and enzymatic implications, *Dalton Trans.*, 2024, **53**(44), 17852–17863.

44 M. Presset, D. Mailhol, Y. Coquerel and J. Rodriguez, Diazo-Transfer Reactions to 1,3-Dicarbonyl Compounds with Tosyl Azide, *Synthesis*, 2011, **2011**(16), 2549–2552.

45 D. F. Taber, P. W. DeMatteo and R. A. Hassan, Simplified Preparation of Dimethyldioxirane (DMDO), in *Organic Syntheses*, John Wiley & Sons, Ltd, 2014, pp. , pp. 350–357, https://onlinelibrary.wiley.com/doi/abs/10.1002/0471264229.os090.33.

46 Y. J. Sun, Q. Q. Huang and J. J. Zhang, Set of Fe(II)-3-Hydroxyflavonolate Enzyme–Substrate Model Complexes of Atypically Coordinated Mononuclear Non-Heme Fe(II)-Dependent Quercetin 2,4-Dioxygenase, *ACS Omega*, 2017, **2**(9), 5850–5860.

47 A. W. Addison, T. N. Rao, J. Reedijk, J. Rijn van and G. C. Verschoor, Synthesis, structure, and spectroscopic properties of copper(II) compounds containing nitrogen–sulphur donor ligands; the crystal and molecular structure of aqua[1,7-bis(*N*-methylbenzimidazol-2′-yl)-2,6-dithiaheptane]copper(II) perchlorate, *J. Chem. Soc., Dalton Trans.*, 1984, (7), 1349–1356.

48 B. Gopal, L. L. Madan, S. F. Betz and A. A. Kossiakoff, The Crystal Structure of a Quercetin 2,3-Dioxygenase from Bacillus subtilis Suggests Modulation of Enzyme Activity by a Change in the Metal Ion at the Active Site(s), *Biochemistry*, 2005, **44**(1), 193–201.

49 R. Rahaman, S. Paria and T. K. Paine, Aliphatic C–C Bond Cleavage of α-Hydroxy Ketones by Non-Heme Iron(II) Complexes: Mechanistic Insight into the Reaction Catalyzed by 2,4′-Dihydroxyacetophenone Dioxygenase, *Inorg. Chem.*, 2015, **54**(22), 10576–10586.

50 A. Banerjee, J. Li, M. A. Molenda, A. A. Opalade, A. Adhikary, W. W. Brennessel, *et al.*, Probing the Mechanism for 2,4′-Dihydroxyacetophenone Dioxygenase Using Biomimetic Iron Complexes, *Inorg. Chem.*, 2021, **60**(10), 7168–7179.

51 L. Jurd and T. A. Geissman, Absorption Spectra of Metal Complexes of Flavonoid Compounds, *J. Org. Chem.*, 1956, **21**(12), 1395–1401.

52 S. Hoof and C. Limberg, The Behavior of Trispyrazolylborato-Metal(II)-Flavonolate Complexes as Functional Models for Bacterial Quercetinase—Assessment of the Metal Impact, *Inorg. Chem.*, 2019, **58**(19), 12843–12853.

53 L. D. Rymbai, K. K. Klausmeyer and P. J. Farmer, The case for an oxidopyrylium intermediate in the mechanism of quercetin dioxygenases, *J. Inorg. Biochem.*, 2023, **247**, 112343.

54 S. Toledo, P. C. Y. Poon, M. Gleaves, J. Rees, D. M. Rogers, W. Kaminsky, *et al.*, Increasing reactivity by incorporating π-acceptor ligands into coordinatively unsaturated thiolate-ligated iron(II) complexes, *Inorg. Chim. Acta.*, 2021, **524**, 120422.

55 D. M. Kurtz, Oxo- and hydroxo-bridged diiron complexes: a chemical perspective on a biological unit, *Chem. Rev.*, 1990, **90**(4), 585–606.

56 M. K. Coggins, S. Toledo, E. Shaffer, W. Kaminsky, J. Shearer and J. A. Kovacs, Characterization and Dioxygen Reactivity of a New Series of Coordinatively Unsaturated Thiolate-Ligated Manganese(II) Complexes, *Inorg. Chem.*, 2012, **51**(12), 6633–6644.

57 K. Ray, S. M. Lee and L. Que, Iron-oxidation-state-dependent O-O bond cleavage of meta-chloroperbenzoic acid to form an iron(IV)-oxo complex, *Inorg. Chim. Acta.*, 2008, **361**(4), 1066–1069.

58 A. R. McDonald and L. Que, High-valent nonheme iron-oxo complexes: Synthesis, structure, and spectroscopy, *Coord. Chem. Rev.*, 2013, **257**(2), 414–428.

59 K. Rydel-Ciszek, T. Pacześniak, I. Zaborniak, P. Błoniarz, K. Surmacz, A. Sobkowiak, *et al.*, Iron-Based Catalytically Active Complexes in Preparation of Functional Materials, *Processes*, 2020, **8**(12), 1683.

60 (*a*) CCDC 2486757: Experimental Crystal Structure Determination, 2025, DOI: 10.5517/ccdc.csd.cc2pgnzt; (*b*) CCDC 2515966: Experimental Crystal Structure Determination, 2025, DOI: 10.5517/ccdc.csd.cc2qg26h.